Insights into Formation and Properties of Templated Dual Mesoporous Titania with Enhanced Photocatalytic Activity

Issam Naboulsi, Bénédicte Lebeau, Laure Michelin, Cédric Carteret, Loic Vidal, Magali Bonne, Jean-Luc Blin

Insights into Formation and Properties of Templated Dual Mesoporous Titania with Enhanced Photocatalytic Activity.

Issam Naboulsi[a], Bénédicte Lebeau[b]*, Laure Michelin[b], Cédric Carteret[c], Loic Vidal[b], Magali Bonne[b], and Jean-Luc Blin[a]*

[a]: Université de Lorraine/CNRS, SRSMC, UMR7565, F-54506 Vandoeuvre-lès-Nancy cedex, France
[b] : Université de Haute Alsace (UHA)/CNRS, Equipe Matériaux à Porosité Contrôlée (MPC), Institut de Science des Matériaux de Mulhouse (IS2M), UMR 7361, F-68093 Mulhouse cedex, France
[c] : Université de Lorraine/CNRS, LCPME, UMR7564, F-54600 Villers-lès-Nancy, France

* Corresponding authors :
Pr. Jean-Luc Blin
Université de Lorraine
SRSMC UMR 7565
Faculté des Sciences et Technologies
BP 70239
F-54506 Vandoeuvre-lès-Nancy cedex, France
Tel. +33 3 83 68 43 70
E-mail: Jean-Luc.Blin@univ-lorraine.fr

Dr. Bénédicte Lebeau
Université de Haute Alsace (UHA), CNRS, Equipe Matériaux à Porosité Contrôlée (MPC), Institut de Science des Matériaux de Mulhouse (IS2M), UMR 7361, ENSCMu
3bis rue Alfred Werner
F-68093 Mulhouse cedex, France
Tel. +33 3 89 33 68 82
E-mail: Benedicte.Lebeau@uha.fr

Abstract

The one pot synthesis of dual mesoporous titania (2.3 and 7.7 nm) has been achieved from a mixture of fluorinated and Pluronic surfactants. The small and the large mesopores networks are templated respectively by a fluorinated-rich liquid crystal and a Pluronic-rich liquid crystal, which are in equilibrium. After calcination at 350°C the amorphous walls are transformed into semi-crystalline anatase preserving the mesoporous structure. Results concerning the photodegradation of methyl orange using the calcined photocatalysts highlight that the kinetic rate constant (k) determined for the dual mesoporous titania is 2.6 times higher than the k value obtained for the mono-modal ones.

Keywords : Titania ; Dual mesoporosity ; Nano-sized walls, Surfactants mixture; Liquid crystals.

1. Introduction

Titania is a semiconductor widely used for its photocatalytic properties, but also as catalyst or as promoter or carrier for metals and their complexes[1-4]. For example, titanium dioxide is the most commonly used catalyst support for gold based catalysis since it allows controlling both the size and the shape of the deposited Au nanoparticles[5]. It also enhances the hydrodesulfurization (HDS) of transition metal sulfides (TMS) by transferring electronic density towards the TMS[6]. However, the low specific surface area of conventional titania limits the loading of the adsorbed active species, involving a low catalytic efficiency[7]. The photocatalytic properties of TiO_2 are due to the fact that when the photons energy of incident light is larger than the band gap of the TiO_2 particles, electrons and holes are generated in the conduction and valence bands, respectively, and migrate to the TiO_2 particle surface[8]. The activity of TiO_2 depends on several parameters such as its crystallographic structure, the particles' size and porosity[9-11]. Since photocatalysis and catalysis are surface processes, a huge literature is devoted to the control of the titania's properties to enhance its activity[12-17]. Among the different characteristics, many efforts are focused on the increase of the specific surface area. To reach this goal, TiO_2 can be dispersed onto porous support with very high surface area such as ordered mesoporous silica and, in that case, the photocatalytic activity of the supported TiO_2 can be considerably superior to that of the powdered TiO_2 particles[18-22]. For example, we have reported the preparation of TiO_2-SiO_2 nanocomposites by the post-synthesis impregnation of a titanium precursor onto SBA-15 silica matrices and subsequent thermal treatment at 400 °C in air[22]. The photoactivity of the prepared materials was evaluated by following the degradation of methyl orange in water under UV irradiation. Results showed that the methyl orange degradation rate in the presence of the composites containing 28 and 44 wt% of crystallized anatase was similar to the one in the presence of commercial fully crystallized anatase[22]. Another approach consists in synthesizing pure

mesoporous titania[15-17]. In that case, thanks to the higher surface area, the access to the active sites is favored[19] and as a consequence the photoactivity efficiency is enhanced. In addition, the continuous particle framework of mesoporous TiO_2 may be also beneficial compared to separate individual nanoparticles, in particular for catalyst recovery and to avoid the toxicity related with the release of nano-sized crystalline particles. Mesoporous titania can be obtained through either hard or soft templating methods. In the case of the hard templating pathway[15-17, 23-26], TiO_2 is the replica of a mould such as ordered mesoporous silica. The main advantage is that the crystallization step to get anatase, which is the most active phase for photocatalysis, can be performed at high temperature since the mould prevents collapse of the mesostructure. Therefore, a benefic effect on the photocatalyst efficiency is noted[24]. However, this procedure is time consuming, non eco-friendly (it usually requires hydrofluoric acid to remove the hard template) and it is quite difficult to completely fulfill the mesopores of the hard template with the titania precursor. The soft templating route[15-17,23,27-31] is based on the co-assembly of the titania precursor and surfactant, as made for the synthesis of ordered mesoporous silica. Nevertheless, the main difficulty is to control the alkoxide precursor hydrolysis and condensation that are much faster than for silicon. To reach this goal, different strategies have been developed and for example this control can be achieved by the use of mixed inorganic precursor or hydrolysis controlling agents, such as acetylacetone, or hydrogen peroxide[27-29]. However, one main drawback still persists. It concerns the limitation of the crystallization temperature around 400°C, which is far under the required temperature (550°C) to completely transform amorphous TiO_2 into anatase. Because of the important role of titania in catalysis and photocatalysis, as reminded above, up to now many efforts are still devoted to the synthesis of mesoporous titania with enhanced efficiency[32-34]. Besides the control of the specific surface area, another trend to improve the performances of the mesoporous TiO_2 catalysts deals with the introduction of a second level of porosity. Indeed, the hierarchal

combination of pores can reduce transport limitations and blockage, resulting in higher activities and better control over selectivity[35]. For example, Yuan et al. shows that, thanks to this property, Pd/Al_2O_3 catalyst with a macro-mesoporous network exhibits higher activity and hydrogenation selectivity than the commercial catalyst[36]. If in literature hierarchical macro-mesoporous titania have also been obtained by using different strategies[37-41] such as the combination of particles agglomeration and the sol gel process[37], or by polymer-induced phase separation[38] to create the macropore network, few reports deals with meso-mesoporous TiO_2 catalysts[42-46], and to the best of our knowledge, none of them talk about the soft templating pathway by using surfactant mixtures as template. Indeed, Lee et al. have reported the synthesis of bimodal mesoporous titania (first pore size ≈ 4-5 nm and the second one ≈50 nm) through the replication of citric acid-templated mesoporous silica, composed of silica-nanospheres framework[42]. Zhao et al. used hexagonal anatase TiO_2-SiO_2 nanocomposites as precursor to give birth to the second mesopore networks *via* an etching method. The pore size distribution shows two peaks at 2.5 nm (secondary network) and at 4.5 nm (primary network)[43]. Bimodal porous titania with small mesopore in the range 2-30 nm and large macro-mesopores between 50-80 nm have been obtained by Chen et al. from Ilmenite ($FeTiO_3$) precursor[44]. The formation of the bimodal titania from $FeTiO_3$ implies different steps: ball milling of the precursor with activated carbon, annealing, leaching by acid and finally calcination in air. Zhang et al.[45] used a mixture of polyethylene glycol and P123 to prepared mesoporous titania with two mesopore sizes (5.5 and 8.7 nm). The obtained mesoporous materials exhibit low specific surface area around 80 m^2/g and taking into account the error on the measurement no significant variation is detected between materials prepared from the pure PEG 6000, the pure P123 and the P123/PEG600 mixture. The same trend is noted concerning the particle's size. In addition, the mesoporosity does not arise from a template effect but it is rather due to the calcination process ant that it can be attributed to an

interparticular porosity. More recently based on a multi-templating approach based on a solo nonionic surfactant P123 and peroxotitanic acid, Ru et al. have prepared bimodal meso-mesoporous titania[46]. The authors assume that under their conditions at high concentration some P123 micelles coalesce. These coalesced micelles are responsible of the formation of the larger mesopore size. As a result, the recovered porous TiO_2 exhibits two mesopores sizes. The first one at around 7 nm arises from the P123 micelles and the second one at higher values (between 10 and 16 nm, depending on the synthesis conditions) is due to the coalesced micelles[46]. However, no detailed investigation has been performed to support this mechanism. In addition, the pore size distributions are very broad and the two maxima clearly appear only when the BJH method is applied on the desorption branch of the isotherm.

A versatile method to get meso-mesoporous materials consists in using surfactant mixtures[47-52]. In particular, thanks to the difference in polarity between the hydrocarbon and fluorocarbon, chain mixtures of hydrogenated and fluorinated surfactants are well adapted for the synthesis of such materials and this methodology has been applied to the preparation of meso-mesoporous silica[50-52]. Here, we combined this approach with the synthesis route that our group has developed for the synthesis of order mesoporous titania with semi-crystalline framework[53,54] to design dual mesoporous titania templated by polyoxyethylene fluoroalkyl ether [$R^F_8(EO)_9$]/ P123 mixtures. After surfactants removal the recovered porous materials were completely characterized by SAXS, TEM, DRX, Manometry nitrogen adsorption/desorption, ATG, UV. The beneficial effect of the presence of the two mesopores for photocatalysis has been demonstrated by evaluating the capacity of the obtained materials to photo-degrade the methyl orange.

2. Materials and methods

2.1. Materials preparation: Mesoporous TiO_2 has been synthesized using mixtures of $R^F_8(EO)_9$ and P123 as templates via the sol-gel method combining the approaches developed by our group to prepare dual mesoporous silica materials[52] and ordered mesoporous TiO_2 with semi-crystalline walls[53-54]. Samples are designed as Px/F100-x where x is the weight content in percent of Pluronic in the surfactant mixture. To transform the amorphous walls into semi-crystalline anatase particles a calcination was carried out at 350°C during one hour under oxygen. To reach this temperature samples have been heated at 1°C/min under nitrogen with a temperature level of one hour at 150°C.

2.2. Characterization : After synthesis, the dual mesoporous titania have been characterized by SAXS, TEM, DRX, Manometry nitrogen adsorption/desorption, ATG, UV. Detailed techniques about the equipments used and analysis procedures are given in references 54-56.

The photocatalytic efficiency of the obtained titanium oxides has been estimated according to a methodology that we have previously reported[57].

3. Results and discussion

3.1. Evidence of the coexistence of the two mesopores networks

After extraction of the surfactant, the SAXS pattern (Fig. 1A) of the material prepared with the pure $R^F_8(EO)_9$ is characteristic of a wormhole-like structure since only one broad reflection is observed at 5 nm (Fig. 1A). Even if there is no pore ordering, this kind of pattern indicates that the channels have a regular size. The position of the peak gives an indication of the average pore-pore distance in the disordered wormhole framework, which lacks long-range crystallographic order. By contrast, the peaks corresponding to d-spacings of 10.8 and 6.3 nm (Fig .1A) detected on the SAXS pattern of the materials templated by the pure P123 copolymer can be attributed to (100) and (110) plane reflections that indicate a hexagonal

mesopore ordering with a cell parameter a_0 of 12.5 nm ($a_0 = 2\ d_{100}/\sqrt{3}$). Looking at the SAXS patterns of the materials prepared from the $R^F_8(EO)_9$/P123 mixture, besides the peak corresponding to a d-spacing of 5.4 nm, a supplementary reflection corresponding to a d-spacing of 14. 3 nm appears when the P123/$R^F_8(EO)_9$ weight ratio reaches 20/80. This indicates the presence of a second mesopores network. Increasing the Pluronic content, the intensity of this reflection also increases, while the one corresponding to the d-spacings of 5.4 nm decreases. For P40/F60, a third reflection corresponding to a d-spacing of about 7 nm appears and its relative position with respect to the first one, characterizes a hexagonal channel array. Thus, a hexagonal network of large pore, characterized by a d-spacing of 14.3 nm for the (100) plane reflection, coexists with a smaller disordered pore network (d-spacing of 5.4 nm for the (100) plane reflection). Beyond 60 wt% of P123 in the surfactant mixture the small mesopores are not clearly observed by SAXS.

After calcination at 350°C, the same trend can be drawn from Figure 1B. However, we can note that the small mesopore network is damaged by the calcination process, whereas the larger one is not significantly affected. Indeed, while no important modification in the pattern is noted for the TiO_2 materials arising from the pure P123, on the one of P0/F100 the broad peak is less resolved, suggesting the beginning of the pore collapse. For both materials, the pore arrangement is confirmed by the TEM images depicted in Figure 2. Indeed, photos of P100/F0 show the hexagonal stacking of the channels or the honeycomb structure whereas for P0/F100 only disordered pores are present (Fig.2A). Even after calcination, as shown by Figures 1B and 2, the coexistence of the two networks is still maintained when porous titania are synthesized from the $R^F_8(EO)_9$/P123 mixtures (Fig. 2A and 2C). In addition, from the lower resolution TEM images depicted in Figure S1, the particle's size has been evaluated to: 220 nm, 211 nm, 237 nm, 176 nm and 330 nm for P100F0, P70F30, P50F50, P30F70 and

P0F100, respectively. From the TEM images, the average sizes of the small and large domains have also been evaluated to 40 nm and 54 nm, respectively.

Nevertheless, a slight contraction of both channel arrays is noted. For example, the d-spacing values of the large and the small mesopores vary from 13.8 and 5.4 nm to 10.9 and 4.5 nm, respectively after calcination of the materials prepared with a P123/$R^F_8(EO)_9$ weight ratio of 30/70. This phenomenon can be attributed to a condensation of the Ti-OH group but also to the crystallization of the walls. Indeed, for all samples, the presence of nano-sized crystallites domains is observed by TEM in dark field (Fig. 2B).

Except the nitrogen adsorption desorption isotherm of TiO_2 prepared from the pure fluorinated surfactant, which is between type I and type IV, all other extracted samples have a type IV isotherm (Fig. 3A), characterizing mesoporous materials according to the IUPAC classification[58]. The isotherm of P0/F100 suggests a supermicroporous materials with mesopore size around 1.8 nm in Fig. 4A. It is interesting to note that reaching a P123/$R^F_8(EO)_9$ weight ratio of 20/80, two inflection points at relative pressure p/p_0 = 0.3 and p/p_0 = 0.7-0.8 are detected on the adsorption branch of the isotherm (Fig. 3A). Since the pore diameter is related to the relative pressure *via* the Kelvin's equation, this reflects the presence of mesopores with two different diameters. Higher the relative pressure at which the capillary condensation occurs, higher the mesopore size is. When the proportion of P123 in the surfactant mixture is raised, the inflection point at p/p_0 = 0.3 gradually disappears (Fig. 3A). So, in the material, the smaller mesopores network becomes a minority. The dual mesoporosity is confirmed by the mesopore size distribution displayed in Figure 4A. In fact, from P30/F70 to P80/F20, two maxima at around 2.3 and 9.7 nm are clearly observed (Fig. 4A). In addition, the ratio between the two mesopores populations is progressively reversed as the Pluronic weight percent in the surfactant mixture increases. At low P123/$R^F_8(EO)_9$ weight ratio the small mesopores predominate while the opposite tendency is noted at high P123

content (Fig. 4A). After calcination at 350°C, the porous materials behave in a similar way (Fig. 3B and 4B). However, shrinkage of the mesopore occurs and the diameter of the small and the large mesopores changes from 2.3 and 7.7 nm to 1.8-2 and 7.7 nm (Table 1). From Table 1 it can also be noted that, upon calcination, both the specific surface area and the mesopore volume decrease. It should be also outlined that with the increase of the P123/$R^F_8(EO)_9$ weight ratio, the total pore volume is enhanced. For example, Vp is changed from 0.16 to 0.5 cm^3/g and from 0.19 to 0.42 cm^3/g when the P123/$R^F_8(EO)_9$ weight ratio is varied from 20/80 to 90/10 after extraction and extraction followed by calcination, respectively. It is also worthy to note that for P30/F70, P50F50, P70/F30, P80/F20 materials after extraction and extraction followed by calcination and for P100/F0 material after extraction the shape of the hysteresis at the desorption in the larger mesopores clearly characterizes a catastrophic desorption of nitrogen at p/p_0 of about 0.5, indicating pores with bottlenecks. For the extracted P100/F0 material, the presence of residual surfactant in mesopores after ethanol extraction can explain this phenomenon. Concerning materials obtained from a mixture of surfactant P123/$R^F_8(EO)_9$, the pore deformations can result from defaults in the P123 liquid crystals due to the presence of $R^F_8(EO)_9$ surfactant molecules. In a general way the specific surface area values are high and they slightly decrease when the P123 content is increased (Table 1).

To explain the formation of these dual-mesoporous materials we should have a look at the $R^F_8(EO)_9$/P123/water phase diagram. In a previous study dealing with the preparation of hierarchical silica materials[52], we have reported that the liquid crystal domain is mainly composed of a biphasic mixture of one fluorocarbon-rich H_1^F in equilibrium with one Pluronic-rich H_1^P hexagonal phase. Here, according to the procedure developed for the synthesis of mono-modal mesoporous TiO_2[53,54], to achieve the one pot preparation of the dual mesoporous titania, the surfactants were first dissolved in a mixture of ethanol and

hydrochloric acid (12N). Then titanium isopropoxide was added before water. After stirring, the mixture was placed under vacuum to evaporate the solvent and the propanol produced during the hydrolysis of the titania precursor. During this step, two organic-inorganic mesophases, one templated by H_1^F and the other by H_1^P, are formed. During the treatment under ammonia atmosphere, the condensation of titania source occurs both around the two kinds of liquid crystals. After surfactant removal, dual-mesoporous materials having two mesopores networks are obtained. However, the quantity of titanium isopropoxide is likely not optimum to get two ordered mesopores networks. This hypothesis is supported by results previously reported in the literature[54,59] about the formation of mono-modal mesoporous TiO_2. For example, in a paper dealing with the preparation of wormhole-like mesoporous titania by using P123 as surfactant and tetrabutyl orthotitanate (TBOT) as titanium source, Hung et al.[59] have reported that the wormhole-like structure is recovered only for P123/TBOT molar ratios located in the range from 0.013 to 0.025.

3.2. Capacity of the dual mesoporous TiO_2 for the photodegradation of methyl orange

Since the photoactivity depends on the crystallographic structure of TiO_2, before performing the photocatalysis tests, the one of the nano-sized crystallite domains appeared after calcination has been identified both by Raman and XRD. Raman spectra of all samples exhibit a very intense band at 150 cm^{-1} and three other vibrations at 394, 506 and 630 cm^{-1}. They can be attributed to E_g, B_{1g}, A_{1g} or B_{1g}, and E_g modes, respectively of anatase. The position of the first band can be correlated to the size of the particles. Indeed, in bulk anatase, this mode appears around 143 cm^{-1} and it is shifted towards higher wavenumber in nanocrystalline materials[60,11]. So, here we can conclude that after crystallization the wall of the dual mesoporous materials are semi-crystalline. The position of Eg indicates that the crystallites' size is below 10 nm[60,11]. The presence of the anatase is further confirmed by

Figure 5B, which depicts the diffractograms of the samples. Peaks characteristic of anatase are clearly detected. Applying the Scherrer formula[61], the mean size of the crystalline domains [D = 0.9 λ/(w cosθ), w is the width at half maximum of the (101) peak] has been estimated between 3 and 5 nm. This value is in accordance with the nano-size suggested by the position of the Eg vibration on the Raman spectra and with the TEM images in dark field reported Figure 2B. However, two broad reflections having a very low intensity, at around 2θ =30 and 2θ = 44°, are also observed and attributed to the presence of amorphous TiO_2. Therefore, from XRD and Raman analyzes, the particles observed by TEM in dark field (Fig. 2B) can be identified as anatase. As a consequence, one can expect that the dual mesoporous titania exhibit a photocatalytic activity. Indeed, the photocatalytic activity of TiO_2 is one of its distinctive features, mainly attributed to its anatase phase.

For photocatalysis, another parameter that should be considered is the band gap energy value, which can be deduced from the UV spectra (Fig. 6A). The UV-Vis spectra of all the synthesized materials exhibit a broad band that can be decomposed in two parts. The first contribution at around 225 nm arises from a ligand to metal charge transfer transition in isolated TiO_4 units. It corresponds to the band transition from Ti 3d to O 2p levels. The second contribution at 320 nm corresponds to small TiO_2 clusters. The energy band gap (E) can be evaluated[54,55] using the Kubelka–Munk formalism. The graphs obtained for P0/F100, P50/F50 and P100/F0 are given as examples in Figure 6B. Except the mesoporous titania prepared from P0/F100, which has a bang gap at 2.6 eV, no significant change of E is noted with the increase of the Pluronic content. As a matter of fact, for the dual mesoporous titania, E remains around 2.9-3.0 eV (Fig. 6C), value closed to the one of the pure anatase, which is 3.2 eV.

Then, the mesoporous titania have been tested for the photo-degradation of methyl orange (MeO), used as a model dye. The degradation of the colorant as a function of irradiation time

is shown on Figure 7A. Looking at the mono-modal materials a slightly higher activity is observed for the TiO_2 templated by pure P123. Indeed, after 210 minutes 70 and 75 % of the dye are degraded by P0/F100 and P100/F0, respectively. Both photocatalysts have semi-crystalline framework with anatase particles between 3 and 5 nm. As a consequence, this difference can be related to the smaller pore diameter (2.0 versus 7.7 nm) and the smaller pore volume of the porous TiO_2 prepared from the pure fluorinated surfactant. Indeed, considering the size of methyl orange, 1.5 nm x 0.55 nm [62], it can also be assumed that its diffusion inside the channel of P0/F100 is not facilitated and that a partial pore blocking occurs. The lower value of the bang gap (2.6 versus ≈ 3.0 ev) is also an unfavorable parameter for photocatalysis under UV radiation.

Whatever the P123/$R^F_8(EO)_9$ weight ratio, it is clear from Figure 7A that the dual mesoporous titania exhibit a higher activity than the mono-modal ones. Indeed, while 90% of the colorant are removed within 180 minutes when P20/F80 is used as catalyst, 60 and 76% of methyl orange are photo-degraded in the same period by P0/F100 and P100/F0, respectively. The degradation efficiency reaches around 95% after180 minutes under UV light for P50/F50 and P60/F40. These dual mesoporous TiO_2 are therefore about 1.5 times more efficient than the mono-modal ones. Using a model of pseudo-first-order reaction [57] the degradation rate (k) has been calculated (Fig. 7B). Both mono-modal mesoporous TiO_2 have a similar k value around $5x10^{-3}$ min^{-1}, suggesting that the lower mass transfer ability of P0/F100 can be partially compensated by the beneficial effect of higher specific surface area on the photodegradation efficiency. Indeed, a larger surface area provides more active sites for adsorbing methyl orange molecules and consequently the two photocatalysts show similar activity.

The variation of k with the P123/$R^F_8(EO)_9$ weight ratio can be divided into two parts (Fig. 7B). It increases as a function of the Pluronic content in the surfactant mixture, used to synthesized the dual mesoporous titania, to reach a maximum value of $1.3x10^{-2}$ min^{-1} for the

P50/F50 and P60/F40 catalysts; i.e. 2.6 times higher than for the mono-modal mesoporous TiO_2. After that, the rate constant gradually decreases. To shed some light about these variations, we have also considered the density of OH groups at the surface of the photocatalysts. Indeed, the photodecomposition of the organic compounds implies the formation of radicals $OH^{\bullet}$, which are created by the reaction at the catalysts' surface of holes with the hydroxyl groups and the catalyst's performances can be correlated to the number of OH groups at the surface[63]. The OH surface density in the porous TiO_2 was calculated from the thermogravimetric curves (not shown) by considering the weight loss (Δm) that occurs after the desorption of both the water molecules physisorbed at the surface of titania and the strongly bound water on titania. The latter are mostly desorbed at around 250°C and completely by 300°C under static air[64]. The OH surface density of the mesoporous TiO_2 can be calculated from the following equation :

$$OH\ (/nm^2) = \frac{\Delta m\ 2\ N_A}{S_{BET}\ m\ M_{H_2O}}$$

where m, S_{BET}, N_A and M_{H2O} stand for the weight of samples, the specific surface area, the Avogadro's number and the molecular weight of water, respectively. From Figure 8, which depicts the values of OH surface density, it is observed that the concentration of OH groups increases as a function of the P123/$R^F_8(EO)_9$ weight ratio to reach the density obtained for a fully hydroxylated TiO_2 surface[64,65], which is around 12-14 OH/nm² for P50/F50 then it remains almost constant.

From P0/F100 to P60/F40, the enhancement of the photocatalysts efficiency observed with TiO_2 synthesized from the surfactants mixtures can be related to both the increase of the OH density from 4 OH/nm² for P0/F100 to around 13 OH/nm² for P60/F40, which favors the formation of radicals $OH^{\bullet}$ at the photocatalyst's surface[62] and to the presence of the dual mesoporosity. Indeed, it should be reminded that SAXS and nitrogen adsorption desorption

analyses have evidenced that two mesopores networks coexist in the porous titania up to a P123/$R^F_8(EO)_9$ weight ratio of P60/F40 and that the proportion of the large mesopores increases from P0/F100 to P60/F40. Therefore, for these catalysts, the wormhole-like network templated by the fluorinated-rich liquid crystal and the ordered mesopore network, induced by the P123-rich liquid crystal, have a synergic effect. They favour the diffusion of the dye molecules inside the channels and their accessibility to the anatase crystallites, which are the active sites. The larger mesopores also contribute to reduce the limitation of the transport of the methyl orange molecules and provide more pathways for products to escape[42-46,66].

From the results reported here, one question arises: can similar results be obtained simply by mixing the two mono-modal TiO_2 with different pore sizes? To answer this question, we have prepared a catalyst by mixing 50% of P0/F100 with 50% of P100/F0. The mixture has been then grinded in an agate mortar. The obtained composite exhibits a type IV isotherm and a pore size distribution with two maxima at 1.8 and 7.7 nm (Fig. 9). They correspond to the diameter of the materials templated by pure $R^F_8(EO)_9$ and pure P123. The specific surface area, the mesopore volume and the band gap are 340 m^2/g, 0.25 cm^3/g and 2.95 eV, respectively. So the features of the obtained material are similar to the ones of P50/F50. From Figure 7A and 7B, it is interesting to note that even if its efficiency for the degradation of methyl orange is higher than the one of the mono-modal mesoporous TiO_2, 90% of the dye removed within 210 minutes and 84% within 180 minutes, it is lower than the one of the dual mesoporous catalysts prepared in one pot by using the $R^F_8(EO)_9$/P123 surfactants mixtures (95% for P50/F50). In addition, the constant rate determined for P50/50 is 1.3 higher than the one of the composite (circle one Fig. 7B), obtained by mixing P0/F100 and P100/F0. This means that, when preparing through the one pot procedure, the two mesopores networks are likely connected (Fig. 2C).

From P60/F400 to P1000/F0, a decrease of the kinetic constant is noted. It cannot be due to a decrease of the OH density, which is constant. Looking at the different parameters this behaviour should be rather correlated to both the progressive disappearance of the small mesopore networks and to a decrease of the specific surface area. Indeed, from the SAXS and nitrogen adsorption-desorption analysis it has been observed that beyond 60 wt.% of Pluronic, the smaller mesopore networks disappears and in the meantime the specific surface area progressively decreases to reach 250 m^2/g for P100/F0, i.e about 100 m^2/g less than P50/F50.

4. Conclusions

The one pot synthesis of dual mesoporous titania have been performed by using mixtures of polyoxyethylene fluoroalkyl ether $R^F_8(EO)_9$ [$C_8F_{17}C_2H_4(OCH_2CH_2)_9OH$] and Pluronic P123 [$(EO)_{20}(PO)_{70}(EO)_{20}$] liquid crystals as templates. SAXS results show that a wormhole-like channel array of small mesopores coexists with a hexagonal pore ordering of large mesopores. The dual porosity is confirmed by the mesopore size distribution

Raman and XRD show that the transformation of the amorphous titania walls into nano-sized anatase walls occurs after calcination at 350°C. With the increase of the P123 in the surfactant mixture, used to prepare the dual mesoporous TiO_2, the OH density increases and no significant change of the band gap energy is noted.

The photodegradation of methyl orange highlight that thanks to the coexistence of the two mesopore networks, the dual mesoporous titania are more efficient than the mono-modal mesoporous ones. Indeed, within 180 minutes, they able to degrade 1.5 times more methyl orange molecules than the mono-modal mesoporous TiO_2. The degradation constant rate is also 2.6 times higher.

The dual mesoporous TiO_2 are therefore of interest for wastewater treatment and air purification. Besides this, it is also expected that the obtained materials have potential

applications in heterogeneous catalysis, for example as support for sulfided CoMo catalysts, which are active for hydrodesulfurization.

Supporting Informations: This information is available free of charge via the Internet at http://pubs.acs.org/. TEM images with lower resolution (S1).

Funding Sources : There is no funding to report for this submission.

Acknowledgments

We would like to thank DuPont de Nemours Belgium for providing the fluorinated surfactant.

References

1 Bai, Y.; Mora-Seró, I.; De Angelis, F.; Bisquert, J.; Wang, P. Titanium Dioxide Nanomaterials for Photovoltaic Applications. *Chem. Rev.*, **2014**, *114*, 10095-10130.

2 Ma, Y.; Wang, W.; Jia, Y.; Chen, X.; Han, H.; Li, C. Titanium Dioxide-Based Nanomaterials for Photocatalytic Fuel Generations. *Chem. Rev.*, **2014**, *114*, 9987-10043.

3 Hadjiivanov, K.I.; Klissurski, D.G. Surface Chemistry of Titania (Anatase) and Titania-supported Catalysts. *Chem. Soc. Rev.*, **1996**, *25*, 61-69.

4 Carp, O.; Huisman, C.L.; Reller A. Photoinduced Reactivity of Titanium Dioxide. *Prog. Solid State Chem.*, **2004**, *32*, 33-177.

5 Panayotov, D.A.; Morris, J.R. Surface Chemistry of Au/TiO_2 : Thermally and Photolytically Activated Reactions. *Surf. Sci. Rep.*, **2016**, *71*, 77-271.

6 Castillo-Villalón, P.; Ramírez, J. Spectroscopic Study of the Electronic Interactions in Ru/TiO_2 HDS Catalysts. *J. Catal.*, **2009**, *268*, 39-48.

7 Wang, H.; Cheng, X. Surface Carbon Activated $NiMO/TiO_2$ Catalyst Towards Highly Efficient Hydrodesulfurization Reaction. *Catal. Surv. Asia*, **2015**, *19*, 78-87.

8 Linsebigler, A.; Lu, G.; Yates, J. Photocatalysis on TiO2 Surfaces: Principles, Mechanisms, and Selected Results. *Chem. Rev.*, **1995**, *95*, 735-758.

9 Li, Z.; Hou, B.; Xu, D.; Wu, D.; Sun, Y. Hydrothermal Ssynthesis, Characterization, and Photocatalytic Performance of Silica-Modified Titanium Dioxide Nanoparticles. *J. Colloid Interface Sci.*, **2005**, *288*, 149-154.

10 Kim, D.S.; Han, S.J.; Kwak, S.Y. Synthesis and Photocatalytic Activity of Mesoporous TiO_2 with The Surface Area, Crystallite Size, and Pore Size. *J. Colloid. Interface Sci.*, **2007**, *316*, 85-91.

11 Zhang, W.F.; He, Y.L.; Zhang, M.S.; Yin, Z.; Chen, Q. Raman Scattering Study on Anatase TiO_2 Nanocrystals. *J. Phys. D: Appl. Phys.* **2000**, *33*, 912-916.

12 Chen, X.; Mao, S.S. Titanium Dioxide Nanomaterials: Synthesis, Properties, Modifications, and Applications. *Chem. Rev.*, **2007,** *107*, 2891-2959.

13 Chen, X.; Selloni, A. Introduction: Titanium Dioxide (TiO_2) Nanomaterials. *Chem. Rev.*, **2014,** *114*, 9281-9282.

14 Schneider, J.; Matsuoka, M.; Takeuchi, M.; Zhang, J.; Horiuchi, Y.; Anpo, M.; Bahnemann, D.W. Understanding TiO2 Photocatalysis: Mechanisms and Materials. *Chem. Rev.*, **2014,** *114*, 9910-9986.

15 Li, W.; Wu, Z.; Wang, J.; Elzatahry,A.A.; Zhao, D. A Perspective on Mesoporous TiO_2 Materials. *Chem. Mater.*, **2014**, *26*, 287-298.

16 Bagheri S.; Hir, Z.A.M.; Yousefi, A.T.; Hamid, S.B.A. Progress on Mesoporous Titanium Dioxide: Synthesis, Modification and Applications. *Microporous Mesoporous Mater.*, **2015**, *218*, 206-222.

17 Kimura, T. Evaporation-induced Self-assembly Process Controlled for Obtaining Highly Ordered Mesoporous Materials with Demanded Morphologies. *Chem. Rec.*, **2016**, *16*, 445-457.

18 Dahl, M.; Liu, Y.; Yin, Y. Composite Titanium Dioxide Nanomaterials. *Chem. Rev.*, **2014,** *114*, 9853-9889.

19 Ismail, A.A.; Bahnemann, D.W. Mesoporous Titania Photocatalysts: Preparation, Characterization and Reaction Mechanisms. *J. Mater. Chem.*, **2011**, *21*, 11686-11707.

20 Lihitkar, N.B.; Abyaneh, M.K.; Samuel, V.; Pasricha, R.; Gosavi, S.W.; Kulkarni, S.K. Titania Nanoparticles Synthesis in Mesoporous Molecular Sieve MCM-41. *J. Colloid Interface Sci.*, **2007**, *314*, 310-316.

21 Nguyen Dinh, M.T.; Rajbhandari, P.; Lancelot, C.; Blanchard, P.; Lamonier, C.; Bonne, M.; Royer, S.; Dumeignil, F.; Payen, E. Tuning Hydrodesulfurization Active-Phase Dispersion using Optimized Mesoporous Titania-Doped Silica Supports. *ChemCatChem*, **2014**, 6, 328-338.

22 Besançon, M.; Michelin, L.; Josien, L.; Vidal, L.; Assaker, K.; Bonne, M.; Lebeau, B.; Blin, J.L. Influence of the Porous Texture of SBA-15 Mesoporous Silica on the Anatase Formation in TiO_2-SiO_2 Nanocomposites. *New J. Chem.*, **2016**, *40*, 4386-4397.

23 Zhang, R.; Elzatahry, A.A.; Al-Deyab, S.S.; Zhao, D. Mesoporous Titania: From Synthesis to Application. *Nano Today*, **2012**, *7*, 344-366.

24 Zhang, Z.; Zuo, F.; Feng, P. Hard Template Synthesis of Crystalline Mesoporous Anatase TiO_2 for Photocatalytic Hydrogen Evolution. *J. Mater. Chem.*, **2010**, *20*, 2206-2212.

25 Yue, B.W.; Randorn, C.; Attidekou, P.S.; Su, Z.; Irvine, J.T.S.; Zhou, W. Syntheses, Li Insertion, and Photoactivity of Mesoporous Crystalline TiO_2. *Adv. Funct. Mater.*, **2009**, *19*, 2826-2833.

26 Wang, J.; Bian, Z.; Zhu, J.; Li, H. Ordered Mesoporous TiO_2 with Exposed (001) Facets and Enhanced Activity in Photocatalytic Selective Oxidation of Alcohols. *J. Mater. Chem. A.*, **2013**, *1*, 1296-1302.

27 Tian, B.; Liu, X.; Tu, B.; Yu, C.; Fan, J.; Wang, L.; Xie, S.; Stucky, G.D.; Zhao, D. Self-Adjusted Synthesis of Ordered Stable Mesoporous Minerals by Acid-Base Pairs. *Nat. Mater.*, **2003**, *2*, 159-163.

28 Tian, B.; Yang, H.; Liu, X.; Xie,S.; Yu, C.; Fan, J.; Tu, B.; Zhao, D. Fast Preparation of Highly Ordered Nonsiliceous Mesoporous Materials via Mixed Inorganic Precursors. *Chem. Commun.* **2002**, 1824-1825.

29 Li, H.; Shi, J.L. ; Liang, J. ; Li, X. ; Li, L.; Ruan, M. Synthesis of Well-Ordered Mesoporous Titania Powder with Crystallized Framework. *Mater. Lett.* **2008**, *62*, 1410-1413.

30 Shibata, H.; Ogura, T.; Mukai, T.; Ohkubo, T.; Sakai, H.; Abe, M. Direct Synthesis of Mesoporous Titania Particles Having a Crystalline Wall. *J. Am. Chem. Soc.*, **2005**, *127*, 16396-16397.

31 Cao, S.; Zhao, Y.; Qu, T.; Wang, P.; Guan, S.; Xu, Y. ; Rao, F.; Li Y.; Chen, A.; Iyodac, T. Ordered Mesoporous Crystalline Titania with High Thermal Stability from Comb-like Liquid Crystal Block Copolyme. *RSC Adv.*, **2016**, *6*, 55834-55841.

32 Hossain, Md. K.; Akhtar, U.S.; Koirala, A.R.; Hwang, I.C.; Yoon, K.B. Steam-Assisted Synthesis of Uniformly Mesoporous Anatase and its Remarkably Superior Photocatalytic Activities. *Catal. Today*, **2015**, *243*, 228-234.

33 Zi, S.C.; Chandren, S.; Yuan, L.S.; Razali, R.; Ho, C.S.; Hartanto, D.; Mahlia, T.M.I.; Nur, H. New Method to Synthesize Mesoporous Titania by Photodegradation of Surfactant Template. *Solid State Sci.*, **2016**, *52*, 83-91.

34 Li, J.; Chen, Y.; Wang, Y.; Yan, Z.; Duan, D. and Wang, J. Synthesis; Photocatalysis of Mesoporous Titania Templated by Natural Rubber Latex. *RSC Adv.*, **2015**, *5*, 21480-21486.

35 Coppens, M.O.; Froment, G.F. The Effectiveness of Mass Fractal Catalysts. *Fractals*, **1997**, *5*, 493-505.

36 Zhou, Z.; Zeng, T.; Cheng, Z.; Yuan, W. Diffusion-Enhanced Hierarchically Macro-Mesoporous Catalyst for Selective Hydrogenation of Pyrolysis Gasoline. *AIChE J.*, **2011**, *57*, 2198-2206.

37 Du, K.F.; Yan, M.; Song, H.; Zhang, Y.K. Synthesis of Bimodal Porous Titania Beads and Their Potentialin Liquid Chromatography. *Ind. Eng. Chem. Res.*, **2011**, *50*, 6101-6108.

38 Drisko, G.L.; Zelcer, A.; Wang, X.; Caruso, R.A.; Soler-Illia, G.J. A.A. Synthesis and Photocatalytic Activity of Titania Monoliths Prepared with Controlled Macro- and Mesopore Structure. *ACS Appl. Mater. Interfaces*, **2012**, *4*, 4123-4130.

39 Cao, L.; Chen, D.; Li, W.; Caruso, R.A. Hierarchically Porous Titania Networks with Tunable Anatase: Rutile Ratios and Their Enhanced Photocatalytic Activities. *ACS Appl. Mater. Interfaces*, **2014**, 6, 13129-13137.

40 Fattakhova-Rohlfing, D.; Zaleska, A.; Bein, T. Three-Dimensional Titanium Dioxide Nanomaterials. *Chem. Rev.*, **2014,** *114*, 9487-9558.

41 Liu, Y.; Li, Y.; Wang, Y.; Xie, L.; Zheng, J.; Li, X. Sonochemical Synthesis and Photocatalytic Activity of meso- and macro-porous TiO_2 for Oxidation of Toluene. *J. Hazard. Mater.*, **2008**, *150*, 153-157.

42 Lee, D.W.; Park, S.J.; Ihm, S.K.; Lee, K.H. Synthesis of Bimodal Mesoporous Titania with High Thermal Stability via Replication of Citric Acid-Templated Mesoporous Silica. *Chem. Mater.*, **2007**, *19*, 937-941.

43 Dong, W.; Sun, Y.; Hua, W.; Yao, Y.; Zhuang, G.; Lv, X.; Ma, A.; Zhao, D. Preparation of Secondary Mesopores in Mesoporous Anatase–Silica Nanocomposites with Unprecedented-High Photocatalytic Degradation Performances. *Adv. Funct. Mater.*, **2016**, *26*, 964-976.

44 Tao, T.; Glushenkov, A.M.; Chen, Q.; Hu, H.; Zhou, D.; Zhang, H.; Boese, M.; Liu, S.; Amal, R.; Chen, Y. Porous TiO_2 with a Controllable Bimodal Pore Size Distribution from Natural Ilmenite. *CrystEngComm*, **2011**, *13*, 1322-1327.

45 Shamaila, S.; Sajjad, A.K.L.; Chen, F.; Zhang, J. Mesoporous Titania with High Crystallinity During Synthesis by Dual Template System as an Efficient Photocatalyst. *Catal. Today*, **2011**, *175*, 568-575.

46 Nguyen, D.; Wang, W.; Long, H.; Shan, W.; Li, X.; Fang, M.; Li, M.; Wang, X.; Ru, H. A Facile and Controllable Multi-Templating Approach Based on a Solo Nonionic Surfactant to Preparing Nanocrystalline Bimodal Meso-Mesoporous Titania. *Microporous Mesoporous Mater.*, **2016**, *230*, 177-187.

47 Groenewolt, M.; Antonietti, M.; Polarz, S. Mixed Micellar Phases of Nonmiscible Surfactants: Mesoporous Silica with Bimodal Pore Size Distribution via the Nanocasting Process. *Langmuir*, **2004**, *20*, 7811-7819.

48 Chen, L.; Xu, J.; Zhang, W.H.; Holmes, J.D.; Morris, M.A. Syntheses of Complex Mesoporous Silicas Using Mixtures of Nonionic Block Copolymer Surfactants: Understanding Formation of Different Structures Using Solubility Parameters. *J. Colloid Interface Sci.*, **2011**, *353*, 169-180.

49 Chen, L.; Zhang, W.H.; Xu, J.; Tanner, D.A.; Morris, M.A. Mesopore Constrictions Derived From the Substitutionally Co-Packed SBA-15. *Microporous and Mesoporous Mater.*, **2010**, *129*, 179-188.

50 Xing, R.; Lehmler, H.J.; Knutson, B.; Rankin, S.E. Synthesis and Tuning of Bimodal Mesoporous Silica by Combined Hydrocarbon/Fluorocarbon Surfactant Templating. *Langmuir*, **2009**, *25*, 6486-6492.

51 Michaux, F.; Blin, J.L.; Stébé, M.J. Design of Ordered Bimodal Mesoporous Silica Materials by Using a Mixed Fluorinated-Hydrogenated Surfactant-Based System. *Langmuir*, **2007**, *23*, 2138-2144.

52 May, A.; Stébé, M.J.; Blin, J.L. Hierarchical Meso-Meso and Macro-Mesoporous Silica Templated by Mixtures of Polyoxyethylene Fluoroalkyl Ether and Triblock Copolymer. *Eur. J. Inorg. Chem.*, **2016**, *13-14* ,1998-2005.

53 Zimny, K.; Ghanbaja, J.; Carteret, C.; Stébé, M.J.; Blin, J.L. Highly Ordered Mesoporous Titania with Semi Crystalline Framework Templated by Large or Small Nonionic Surfactants. *New. J. Chem.*, **2010**, *34*, 2113-2117.

54 Zimny, K.; Roques-Carmes, T.; Carteret, C.; Stébé, M.J.; Blin, J.L. Synthesis and Photoactivity of Ordered Mesoporous Titania with a Semicrystalline Framework. *J. Phys. Chem. C*, **2012**, *116*, 6585-6594.

55 Assaker, K ; Lebeau, B ; Michelin, L. ; Gaudin, P. ; Carteret, C. ; Vidal, L. ; Bonne, M ; Blin, J.L. Zn-TiO_2 Mesoporous Oxides Prepared by Mechanical Milling. *J. Alloys Compd.*, **2015**, *649*, 1-10.

56 Assaker, K.; Carteret, C.; Durand, P.; Aranda, L.; Stébé, M.J.; Blin, J.L. Hydrothermal Stability of Ordered Surfactant-Templated Titania. *J. Phys. Chem. C*, **2013**, *117*, 16500-16508.

57 Blin, J.L.; Stébé, M.J.; Roques-Carmes, T. Use of Ordered Mesoporous Titania with Semi-crystalline Framework as Photocatalyst. *Colloids Surf., A*, **2012**, *407*, 177-185.

58 Sing, K.S.W.; Everett, D.H.; Haul, R.A.W.; Moscou, L.; Pierotti, R.A.; Rouquerol, J.; Siemieniewska, T. Reporting Physisorption Data for Gas/Solid Systems with Special Reference to the Determination of Surface Area and Porosity (Recommendations 1984). *IUPAC, Pure Appl. Chem.*, **1985**, *57*, 603-619.

59 Hung, I.M.; Wang, Y.; Huang, C.F.; Fan, Y.S.; Han, Y.J.; Peng, H.W. Effects of Templating Surfactant Concentrations on the Mesostructure of Ordered Mesoporous Anatase TiO_2 by an Evaporation-Induced Self-Assembly method. *J. Eur. Ceram. Soc.*, 2010, **30**, 2065-2072.

60 Kelly, S.; Pollak, F.H.; Tomkiewicz, M. Raman Spectroscopy as a Morphological Probe for TiO_2 Aerogels. *J. Phys. Chem. B*, **1997**, *101*, 2730-2734.

61 Klug, H.P.; Alexander L.E. in *X-ray Diffraction Procedures*, Wiley (eds), New York, 1954, ch. 9.

62 Darmograi, G.; Prelot,B.; Layrac, G.; Tichit, D.; Martin-Gassin, G.; Salles, F.; Zajac, J. Study of Adsorption and Intercalation of Orange-Type Dyes into Mg–Al Layered Double Hydroxide. *J. Phys. Chem. C*, **2015**, *119*, 23388-23397.

63 Carneiro, J.T.; Savenije, T.J.; Moulijn, J.A.; Mul, G. Toward a Physically Sound Structure-Activity Relationship of TiO2-Based Photocatalysts. *J. Phys. Chem. C*, **2010**, *114*, 327-332..

64 El Shafei, G.M.S; Philip, C.A.; Moussa, N.A. Preparation and Characterization of High Surface Area Mesoporous Anatase Obtained From $TiCl_3$ Hydrothermally. *Microporous and Mesoporous Mater.*, **2005**, *79*, 253-260.

65 Mueller, R.; Kammler, K.K.; Wegner, K.; Pratsinis, S.E. OH Surface Density of SiO_2 and TiO_2 by Thermogravimetric Analysis. *Langmuir*, **2003**, *19*, 160-165.

66 Kim, S.S.; Pauly, T.R.; Pinnavaia, T.J. Non-Ionic Surfactant Assembly of Wormhole Silica Molecular Sieves from Water Soluble Silicates. *Chem. Commun.*, **2000**, *10*, 835-836.

Figures caption

Figure 1: SAXS pattern of the porous TiO_2 after extraction of the surfactants (A) and extraction followed by calcination at 350°C (B).

Figure 2 : Representative TEM images of the porous TiO_2 synthesized from $R^F_8(EO)_9$/P123 mixtures after extraction followed by calcination at 350°C. A : TEM images, B: TEM in dark field and C : High magnification.

Figure 3 : Nitrogen adsorption-desorption isotherms of the porous TiO_2 after extraction of the surfactants (A) and extraction followed by calcination at 350°C (B).

Figure 4 : Mesopore size distributions obtained by the BJH method applied to the adsorption branch of the isotherm of the porous TiO_2 after extraction of the surfactants (A) and extraction followed by calcination at 350°C (B).

Figure 5 : Raman spectra (A) and XRD patterns (B) of the porous TiO_2 after extraction followed by calcination at 350°C. * : reflection attributed to amorphous TiO_2.

Figure 6 : Diffuse reflectance UV-Visible spectra (A), example of $(\alpha h\nu)^{1/2}$ versus photon energy (B) and variation of the energy band gap (C), as a function of P123 content, for the porous TiO_2 after extraction followed by calcination at 350°C. On Figure C line is just a guide for the eyes.

Figure 7 : Change in the concentration of methyl orange (MeO) as a function of the irradiation time (A) and variation of the degradation rate (B), as a function of P123 content, for the porous TiO_2 recovered after extraction followed by calcination at 350°C. On Figurer B line is just a guide for the eyes.

Figure 8 : Variation of the OH surface density (OH/nm^2) for the porous TiO_2. Line is just a guide for the eyes.

Figure 9 : Nitrogen adsorption-desorption isotherm (A) and pore size distribution (B) of the titania composite obtained by mixing 50% of P0/F100 with P100/F0.

Table 1 : Specific surface area (S_{BET}), pore volume (Vp) and pore diameter (Ø) as a function of the P123/ $R^F_8(EO)_9$ weight ratio.

	Amorphous porous TiO_2			Porous TiO_2 after calcination		
P123/ $R^F_8(EO)_9$ weight ratio	S_{BET} (m^2)	Vp (cm^3/g)	Ø (nm)	S_{BET} (m^2)	Vp (cm^3/g)	Ø (nm)
P0/F100	370	0.13	2.0	305	0.15	2.0
P10/F90	476	0.25	2.3	375	0.2	2.0
P20/F80	300	0.16	2.7-10.5	253	0.12	2-8.5
P30/F70	306	0.2	2.7-9.7	344	0.19	2.2-9
P40/F60	488	0.38	2.3-9	386	0.26	2-9.7
P50/F50	452	0.42	2.5-8.7	350	0.3	2-7.7
P60/F40	371	0.36	2.2-9.8	292	0.3	1.8-7.6
P70/F30	378	0.5	2.4-8.7	290	0.6	1.8-7.6
P80/F20	394	0.55	2.4-9.2	332	0.45	1.8-7.8
P90/F10	380	0.5	9.0	280	0.42	7.7
P100/F0	310	0.44	9.7	252	0.37	7.7

Figure 1

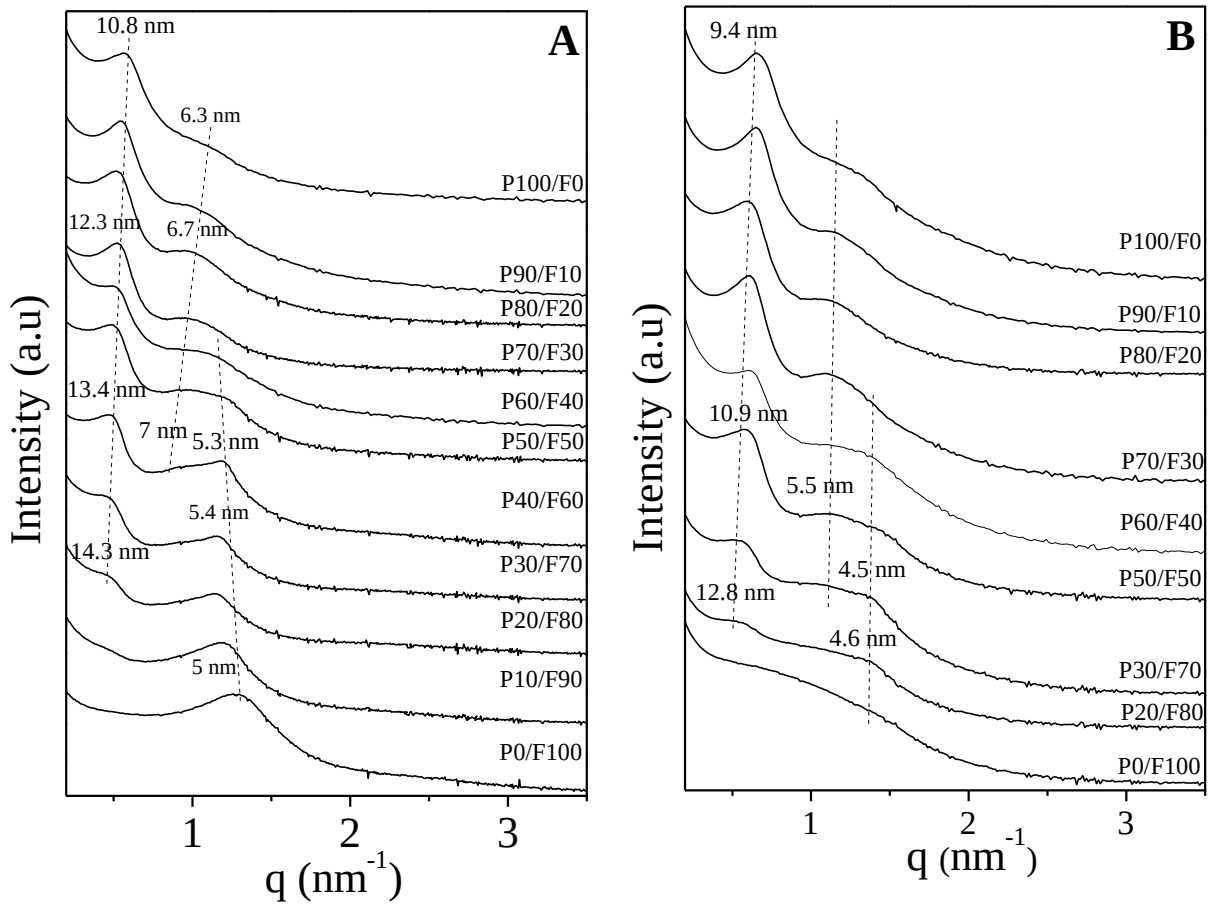
A
10.8 nm
6.3 nm
12.3 nm
6.7 nm
13.4 nm
7 nm
5.3 nm
5.4 nm
14.3 nm
5 nm
P100/F0
P90/F10
P80/F20
P70/F30
P60/F40
P50/F50
P40/F60
P30/F70
P20/F80
P10/F90
P0/F100
Intensity (a.u)
q (nm-1)
B
9.4 nm
10.9 nm
5.5 nm
4.5 nm
12.8 nm
4.6 nm
P100/F0
P90/F10
P80/F20
P70/F30
P60/F40
P50/F50
P30/F70
P20/F80
P0/F100
Intensity (a.u)
q (nm-1)

Figure 2

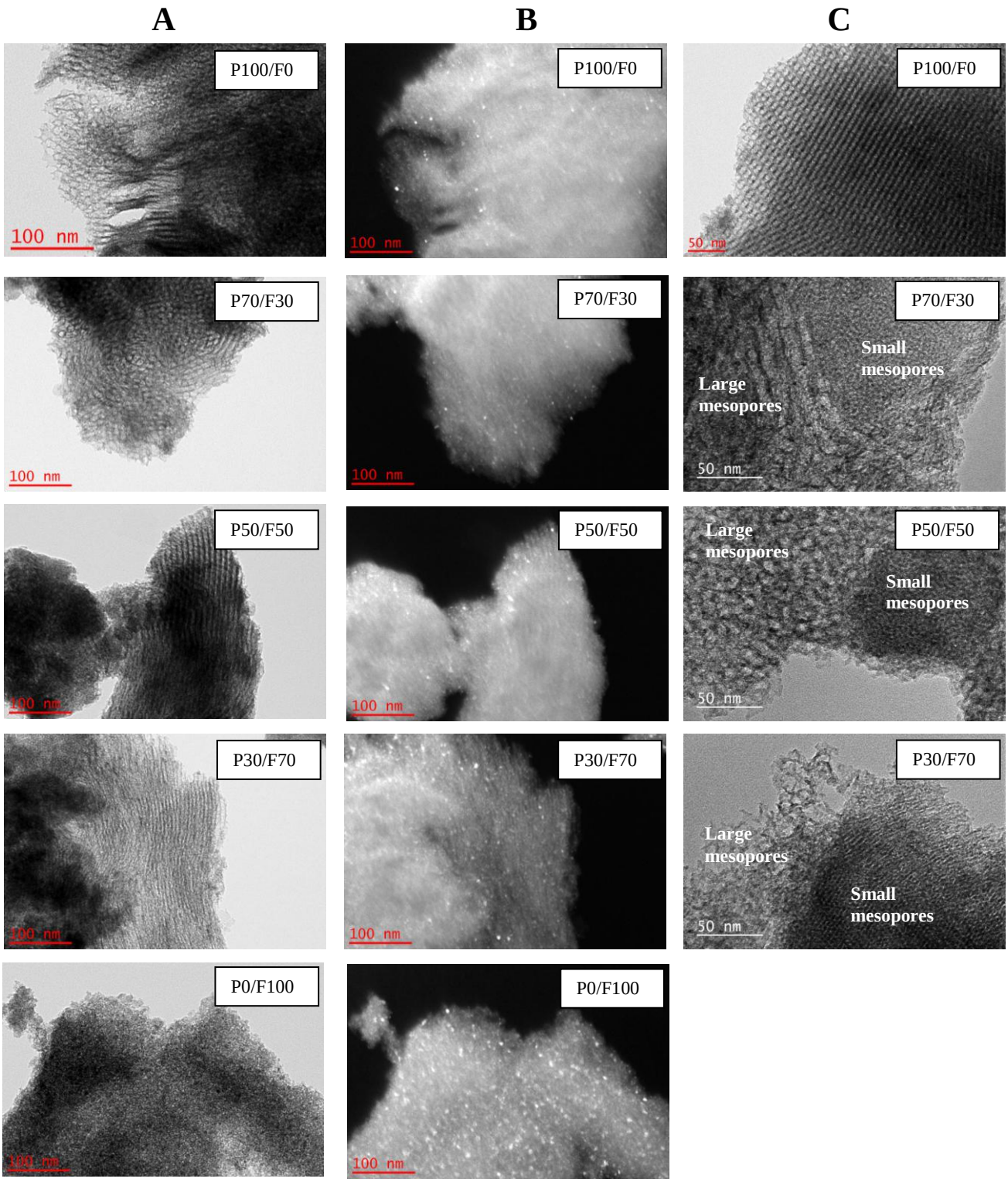
A
B
C
P100/F0
P100/F0
P100/F0
100 nm
100 nm
50 nm
P70/F30
P70/F30
P70/F30
Small mesopores
Large mesopores
100 nm
100 nm
50 nm
P50/F50
P50/F50
Large mesopores
P50/F50
Small mesopores
100 nm
100 nm
50 nm
P30/F70
P30/F70
P30/F70
Large mesopores
Small mesopores
100 nm
100 nm
50 nm
P0/F100
P0/F100
100 nm
100 nm

Figure 3

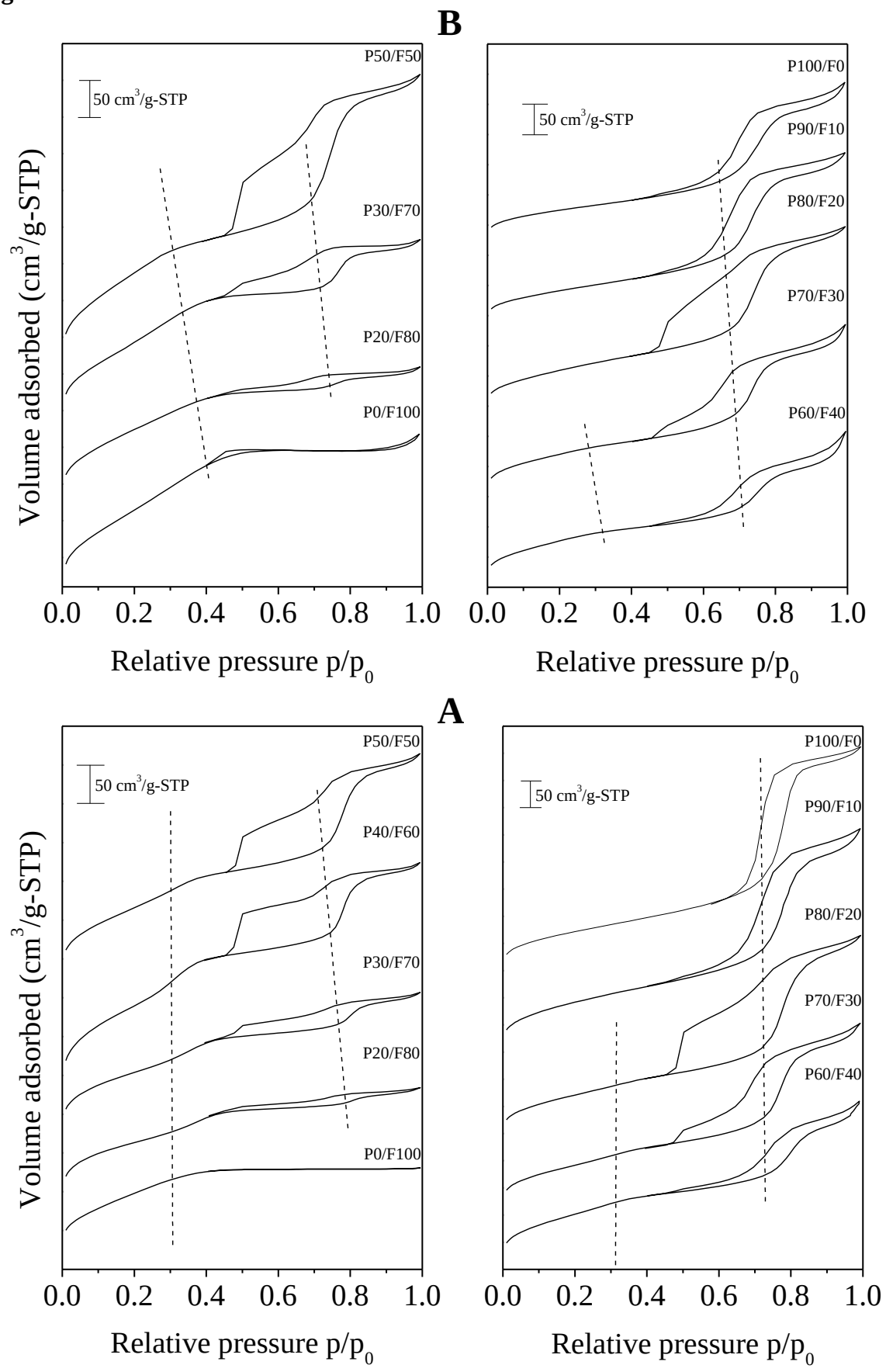
B
P50/F50
50 cm3/g-STP
P30/F70
P20/F80
P0/F100
Volume adsorbed (cm3/g-STP)
0.0 0.2 0.4 0.6 0.8 1.0
Relative pressure p/p0
P100/F0
50 cm3/g-STP
P90/F10
P80/F20
P70/F30
P60/F40
0.0 0.2 0.4 0.6 0.8 1.0
Relative pressure p/p0
A
P50/F50
50 cm3/g-STP
P40/F60
P30/F70
P20/F80
P0/F100
Volume adsorbed (cm3/g-STP)
0.0 0.2 0.4 0.6 0.8 1.0
Relative pressure p/p0
P100/F0
50 cm3/g-STP
P90/F10
P80/F20
P70/F30
P60/F40
0.0 0.2 0.4 0.6 0.8 1.0
Relative pressure p/p0

Figure 4

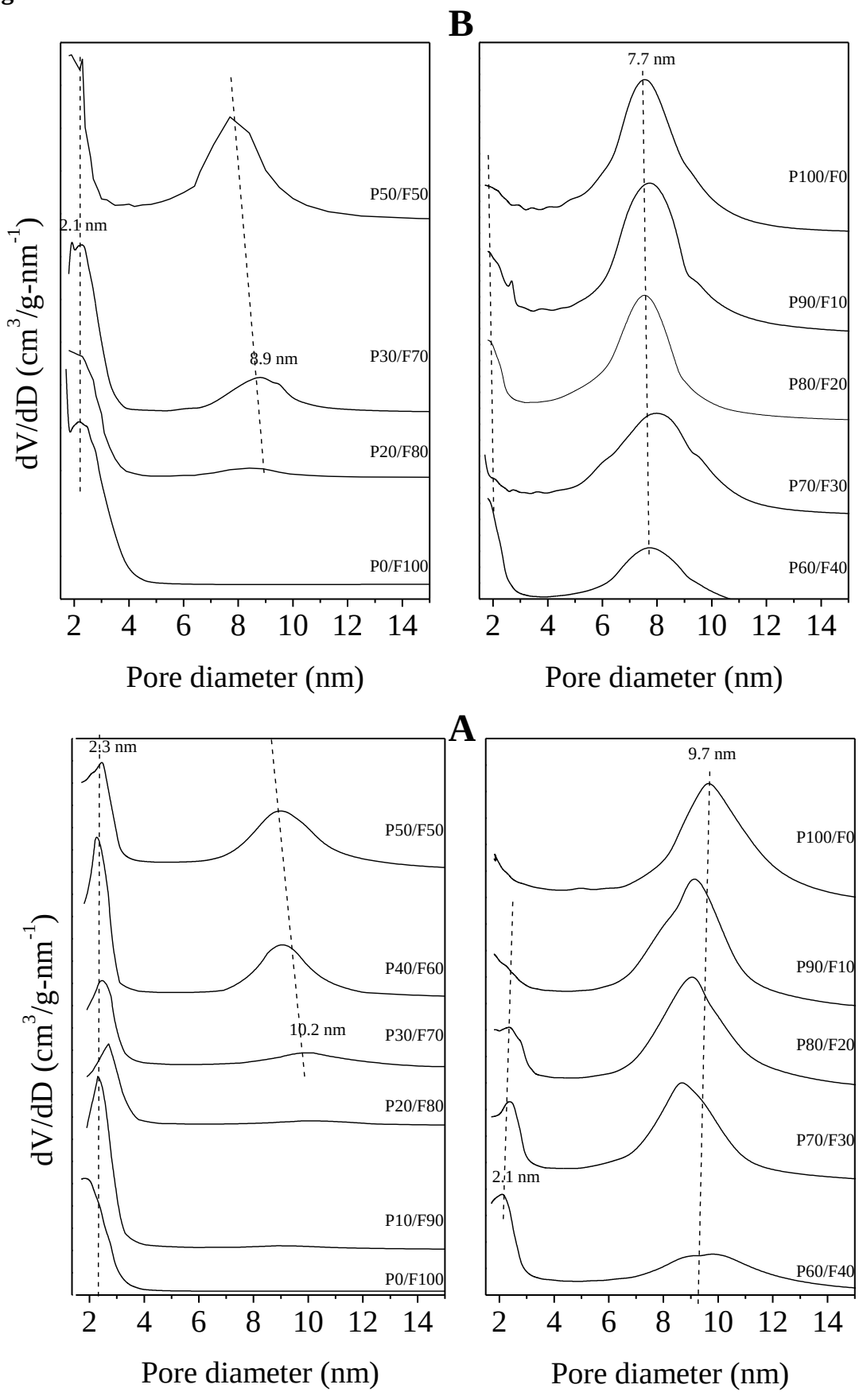
B
7.7 nm
P100/F0
P90/F10
P80/F20
P70/F30
P60/F40
2.1 nm
8.9 nm
P50/F50
P30/F70
P20/F80
P0/F100
dV/dD (cm3/g-nm-1)
2 4 6 8 10 12 14
Pore diameter (nm)
A
2.3 nm
9.7 nm
P50/F50
P40/F60
10.2 nm
P30/F70
P20/F80
P10/F90
P0/F100
P100/F0
P90/F10
P80/F20
P70/F30
2.1 nm
P60/F40
dV/dD (cm3/g-nm-1)
2 4 6 8 10 12 14
Pore diameter (nm)

Figure 5

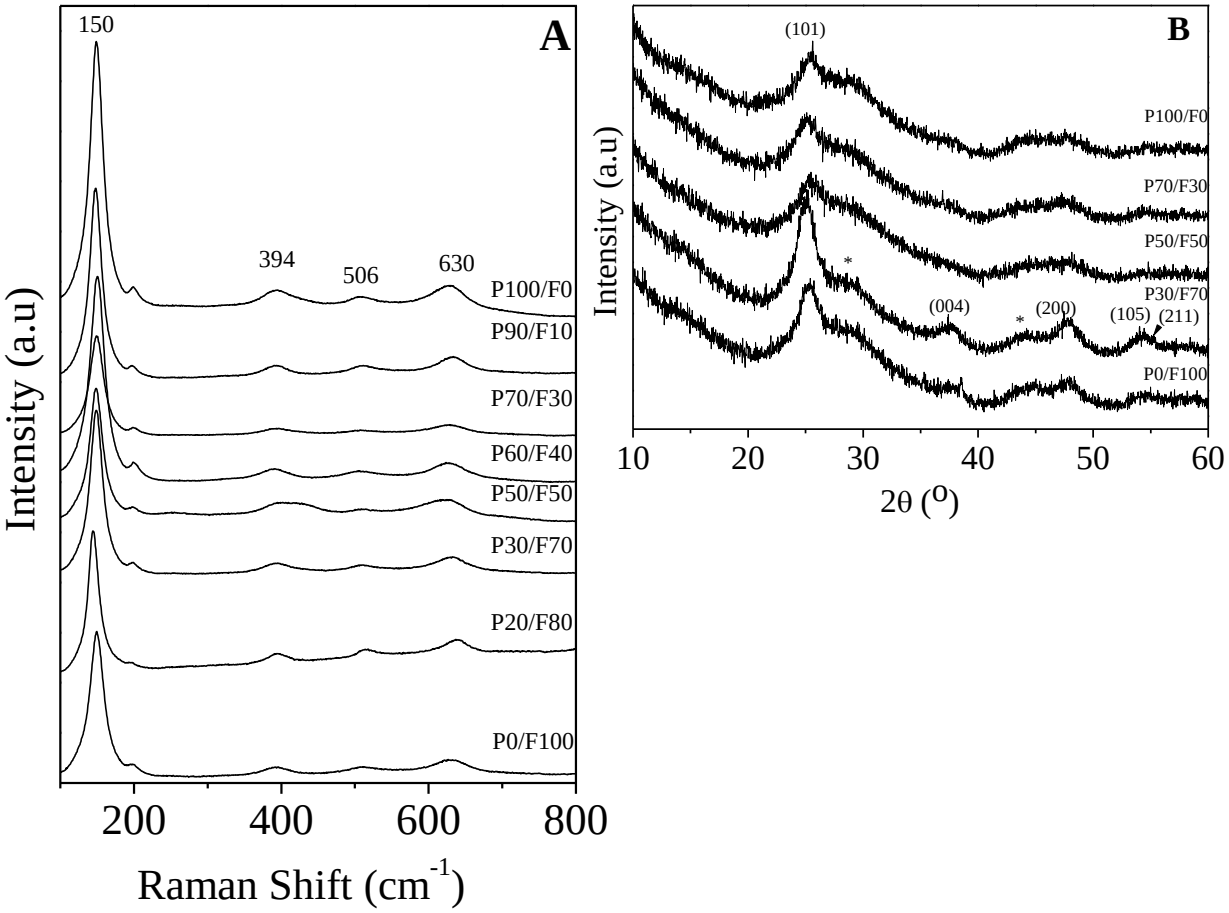
A
150
394
506
630
P100/F0
P90/F10
P70/F30
P60/F40
P50/F50
P30/F70
P20/F80
P0/F100
Intensity (a.u)
200
400
600
800
Raman Shift (cm-1)
B
(101)
P100/F0
P70/F30
P50/F50
P30/F70
P0/F100
(004)
(200)
(105)
(211)
*
*
Intensity (a.u)
10
20
30
40
50
60
2θ (o)

Figure 6

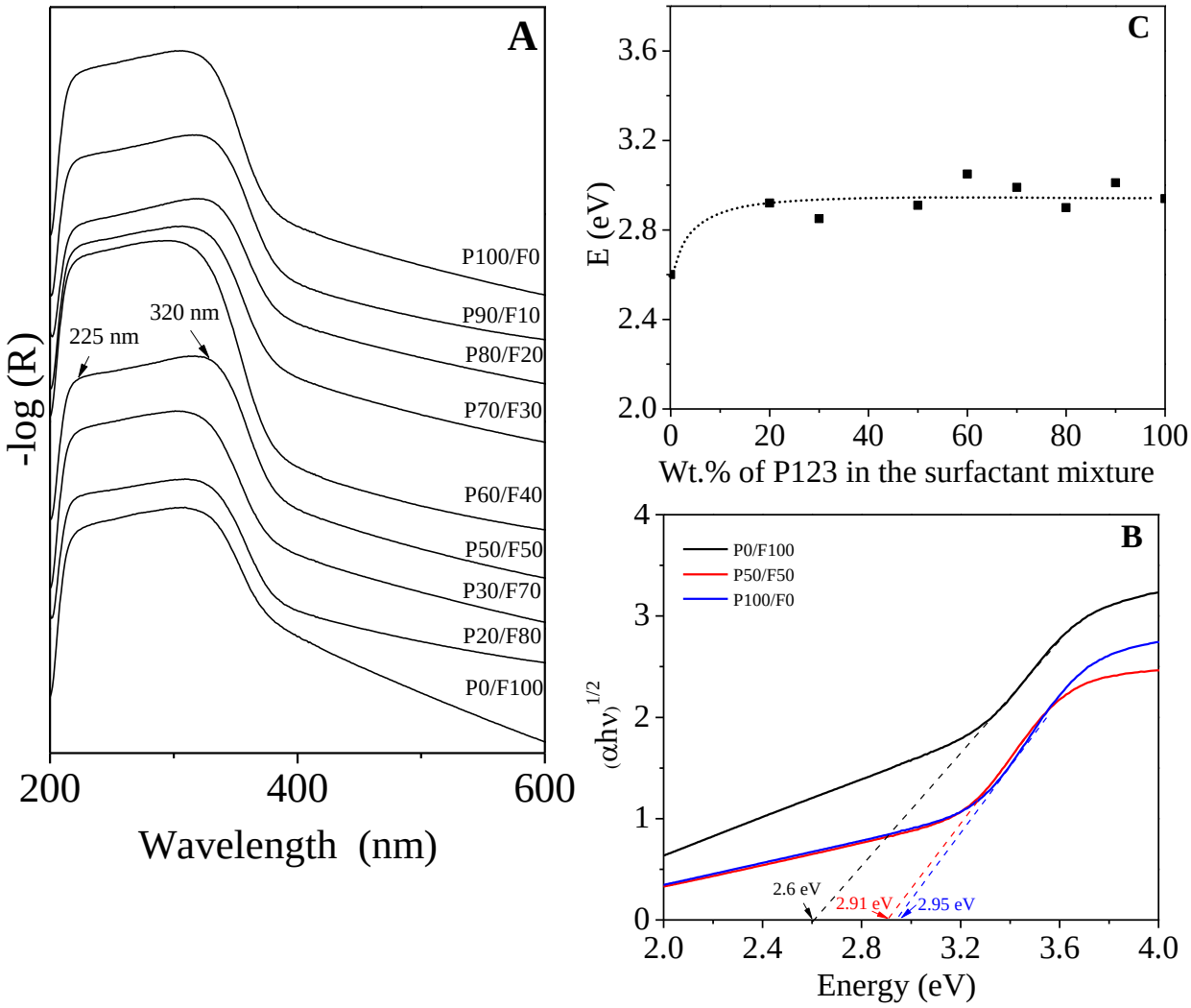
A
-log (R)
320 nm
225 nm
P100/F0
P90/F10
P80/F20
P70/F30
P60/F40
P50/F50
P30/F70
P20/F80
P0/F100
200
400
600
Wavelength (nm)
C
E (eV)
3.6
3.2
2.8
2.4
2.0
0
20
40
60
80
100
Wt.% of P123 in the surfactant mixture
B
P0/F100
P50/F50
P100/F0
(αhν)^1/2
2.6 eV
2.91 eV
2.95 eV
4
3
2
1
0
2.0
2.4
2.8
3.2
3.6
4.0
Energy (eV)

Figure 7

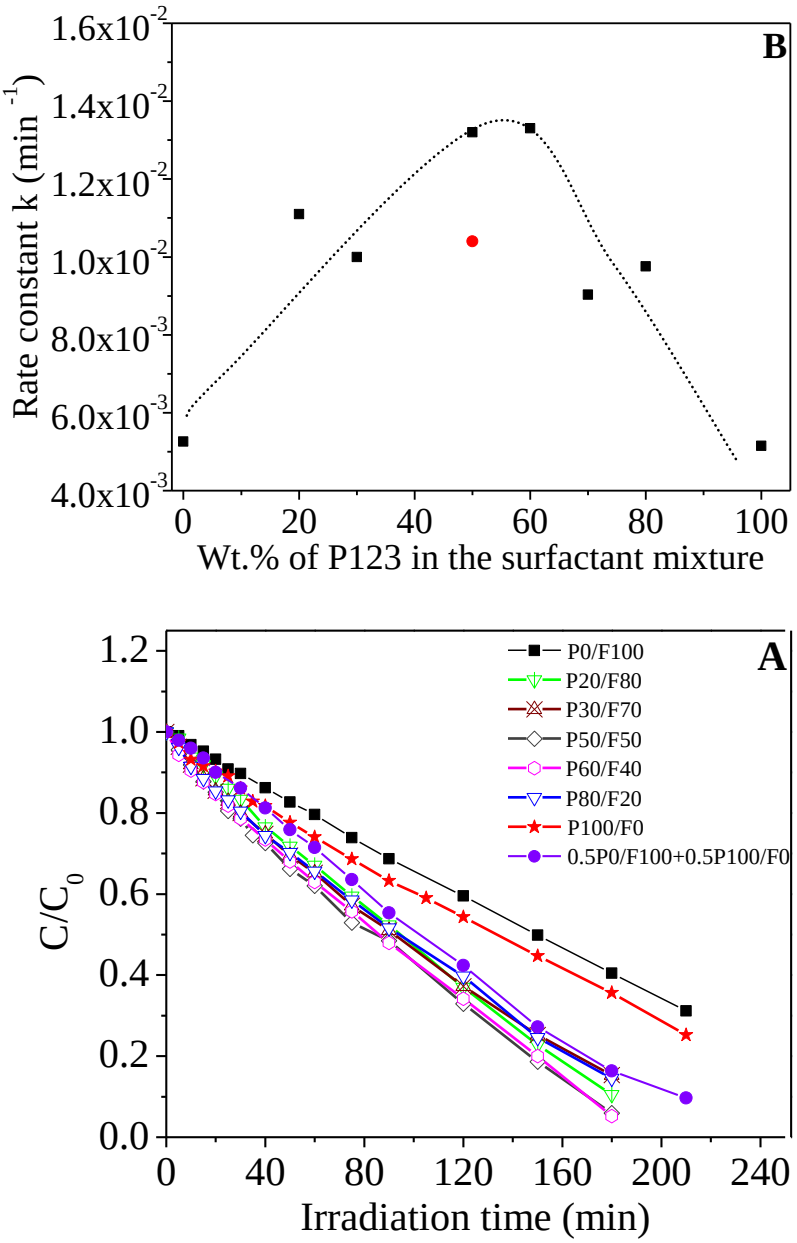
B
Rate constant k (min^{-1})
1.6x10^{-2}
1.4x10^{-2}
1.2x10^{-2}
1.0x10^{-2}
8.0x10^{-3}
6.0x10^{-3}
4.0x10^{-3}
0
20
40
60
80
100
Wt.% of P123 in the surfactant mixture
A
P0/F100
P20/F80
P30/F70
P50/F50
P60/F40
P80/F20
P100/F0
0.5P0/F100+0.5P100/F0
C/C$_0$
1.2
1.0
0.8
0.6
0.4
0.2
0.0
0
40
80
120
160
200
240
Irradiation time (min)

Figure 8

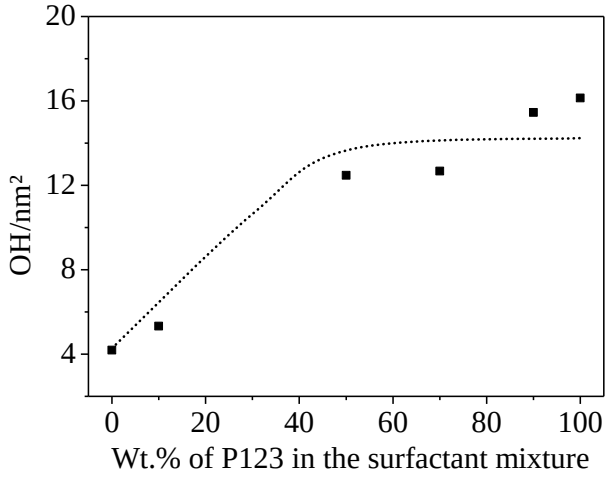
20
16
12
8
4
OH/nm²
0
20
40
60
80
100
Wt.% of P123 in the surfactant mixture

Figure 9

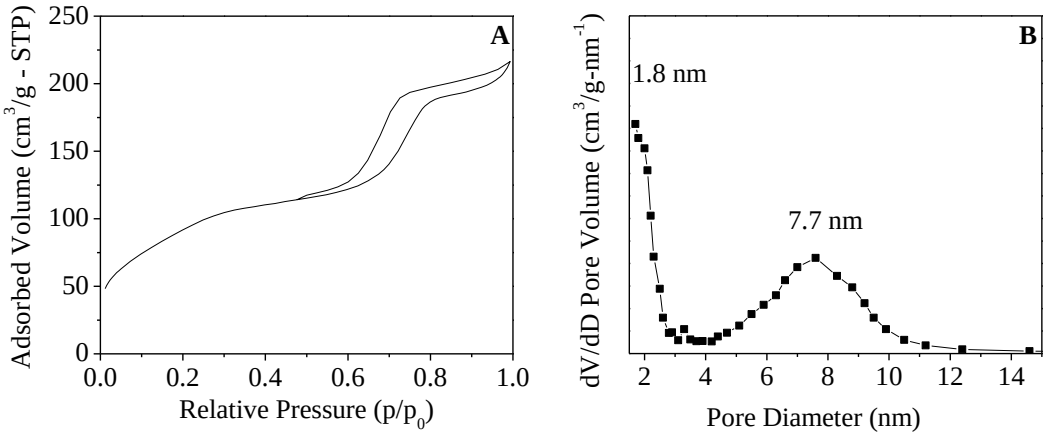
A
Adsorbed Volume (cm3/g - STP)
Relative Pressure (p/p0)
0
50
100
150
200
250
0.0
0.2
0.4
0.6
0.8
1.0
B
1.8 nm
7.7 nm
dV/dD Pore Volume (cm3/g-nm-1)
Pore Diameter (nm)
2
4
6
8
10
12
14

Graphical abstract

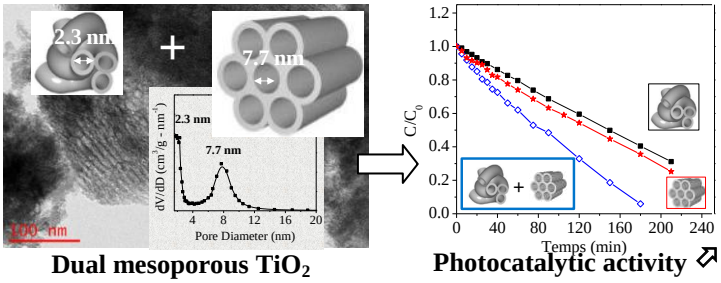

Dual mesoporous TiO_2 **Photocatalytic activity**